

Identifying and diagnosing coherent associations and causalities between multi-channels of the gravitational wave detector

Piljong Jung,¹ Sang Hoon Oh,¹ Young-Min Kim,² Edwin J. Son,¹ Takaaki Yokozawa,³ Tatsuki Washimi,⁴ and John J. Oh^{1,*}

¹*National Institute for Mathematical Sciences, Daejeon 34047, Republic of Korea*

²*Department of Physics, Ulsan National Institute of Science and Technology, Ulsan 44919, South Korea*

³*Institute for Cosmic Ray Research (ICRR), KAGRA Observatory, the University of Tokyo*

⁴*Gravitational Wave Science Project (GWSP), Kamioka branch,
National Astronomical Observatory of Japan (NAOJ)*

(Dated: April 4, 2022)

The gravitational-wave detector is a very complicated and sensitive collection of advanced instruments, which is influenced not only by the mutual interaction between mechanical/electronics systems but also by the surrounding environment. Thus, it is necessary to categorize and reduce noises from many channels interconnected by such instruments and environment for achieving the detection of gravitational waves because it enhances to increase of a signal-to-noise ratio and reduces false alarms from coincident loud events. For this reason, it is of great importance to identify some coherent associations between complicated channels. This study presents a way of identifying (non-) linear couplings between interconnected channels by using some correlation coefficients, which are applied to practical issues such as noises by hardware injection test, lightning strokes, and air compressor vibrations gravitational-wave detector.

I. INTRODUCTION

Since the era of gravitational wave (GW) astronomy was opened by the detection of GW emitted from the binary black hole coalescence (GW150914) [1], it has entered the stage of a leap to pursuit new perspectives on the structure of the Universe and the evolution of astrophysical objects such as stars and galaxies. For more profound understanding and expansion of the knowledge on the Universe, there still exist many challenges to be overcome for GW physics and astronomy. Much more accurate sky localization for GW sources and a much farther range of luminosity distance in GW observation require the improved sensitivity of GW detectors, overcoming the present limitation of technologies.

Detectors' sensitivity confines the boundary of observations so that the number of GW events within the boundary determines the detection rate that can be achieved in the current GW detector. The currently operating ground-based laser interferometric GW detectors such as Laser Interferometer Gravitational-wave Observatory (LIGO), the Virgo, and the KAGRA have a similar design sensitivity curve with a frequency band of $30 - 2000\text{Hz}$, which is characterized by three main noise sources: photon shot noise by the laser system at high-frequency range, thermal noise by test-mass mirrors at mid-frequency range, and seismic noise by ground vibrations at low-frequency range [2–5]. Those GW detectors are now being operated for detecting GW signals and planned for upgrades to improve their sensitivities using many engineering challenges such as cryogenics, quantum squeezed light, and so on. Furthermore, next-

generation ground-based GW detectors with new conceptual designs are now being planned [6, 7].

Besides, advanced methodologies and analysis algorithms should be required to enhance the quality of data [8–10] taken from the very sensitive instruments and isolate GW signals from noises caused by the sensitive devices and the surrounding environments efficiently because it improves the detection statistics such as signal-to-noise ratio (SNR) to provide the reliable detection criterion. This, consequently, also improves the detection range of GW detectors, which yields better detection rates of GW sources. In this point of view, both developments of advanced methodologies for data analysis and understanding the status of GW detectors, as well as the most sensitive instruments, are of special importance to achieve for detecting GW signals coming from the farthest GW emitting objects. For this reason, many different tools for characterizing noises have been developed and utilized for analyzing GW signals so far. The first purpose of those tools is to categorize and classify transient/continuous noises that are harmful to the main GW channel, identifying the interconnected families of noisy channels with the causal relationship. Then they should be mitigated with the help of various advanced mathematical algorithms as is possible. Finally, if they are caused by some instrumental defects with a possibility of repeated malfunctions, the causes should be reported and amended for maintaining the consistent status of the detector.

Many efforts for identifying and vetoing transient noises have been made so far and is widely utilized for GW data analysis, such as a computation of significance called *hierarchical veto* (*Hveto*) [11], Q-transform based trigger generator [12], Hilbert-Huang transform-based method [13], linear regressions [14], machine learning algorithms [15], and so on. These methods cover classi-

* johnoh@nims.re.kr

fication and a vetoing method as well as identification of the influences between the main channel and other auxiliary channels monitoring the environmental and/or instrumental status. This needs consistent understandings of which channel effects can cause the transient noises in the main channel and/or which can be useful to mitigate such abnormalities to maintain the normal status of the detector. However, the GW detector behaves with a highly non-stationary and non-linear nature, we still face great challenges in dealing with noises of GW data.

For this reason, it is necessary to develop more advanced analysis tools for noise hunting to improve the detector's data quality. Here we focus on the couplings and causalities propagated from a certain auxiliary channel to the main GW channel. In Ref. [16], it has been shown that the excess noises from bilinear and non-linear couplings in GW interferometers can be treated using the bilinear coupling veto (BCV) method [17] with the trigger-based correlation coefficient. Along this line, we suggest a new way of identifying coherent associations between GW and the related auxiliary channels, in which we use three kinds of the correlation coefficient: Pearson's correlation coefficient (PCC) [18] and Kendall's τ coefficient (Ktau) [19] as a linear measure and Maximal Information Coefficient (MIC) as a non-linear measure [20–22], respectively. In particular, MIC is an information-theoretic measure to discriminate the nonlinear association between two random variables. Together with these measures, we construct a systematic way of identifying the noises from (non-)linear couplings and causalities propagating from instrumental and/or environmental disturbances of GW detectors. Then we apply the suggested method to the well-known issues of data analysis and noise identification in LIGO and KAGRA detectors.

In this study, we present a way of identifying coherent associations between GW and auxiliary noise channels by computing correlation measures. The method we consider here is the PCC and Ktau as a linear measure, and MIC as a non-linear measure. We construct a consistent way of discriminating the relevant noise effect and its causality, applying to some issues in gravitational wave detection. In Section II, we describe the methods to measure (non-)linear associations and build an analysis process with proper statistical algorithms between GW and many auxiliary channels. In Section III, we exhibit the exemplary results based on some noise data taken from the KAGRA GW detector; a lightning stroke, an air compressor noises, and the noises caused by wind effect. Finally, we summarize and discuss our results in Section IV.

II. METHOD AND WORKFLOW

We use the data with the main GW channel and many auxiliary channels taken from the KAGRA GW detector. The KAGRA is a gravitational-wave detector with

a similar configuration of laser interferometry such as the LIGO/Virgo except for the cryogenic test-mass mirrors and the underground installation [23]. The initial installation of the KAGRA has finished in 2019, and after a year-long commissioning, it started its first observing run during a month in 2020 and joined the O3 observing run together with the advanced LIGO and the Advanced Virgo, recently [24].

The main feature of the KAGRA is the cryogenic and underground GW detector, which implies that the KAGRA detector has somewhat unique characteristics caused by the nature of the underground cryogenic facility, producing the relevant noise effects that are not reported in the ground-based GW detectors. Therefore, it is of great importance to understand the noise characteristic from the KAGRA detector and its environment.

A. Methods for Data Correlations

We introduce three methods of analysis for investigating the correlation of two data samples; the PCC, the Ktau, and the MIC. Let us consider two time-series data X and Y to be non-stationary and uni-variate data sets with equal size of n . We assume that (x_i, y_i) is a set of i -th bi-variate data pair from the paired data (X, Y) . If we assume that the data set Y includes certain noises, being affected the sensitivity of GW detectors, there exist a meaningful statistical association between two observed variables X and Y because the noise propagates to another data set X . With these assumptions, we analyze the correlations and the causalities of noise propagation resulted from the instrumental anomalies and/or environmental causes in gravitational wave detectors. In this section, we describe three major methods to estimate the linear and non-linear associations based on the time-series data recorded in each channel.

The PCC produces the linear correlation score between two variables defined by the ratio between the covariance and the product of standard deviation of each variable. Let $\bar{x} = \sum_{i=1}^n x_i/n$ and $\bar{y} = \sum_{i=1}^n y_i/n$ be the means of X and Y , respectively. Then, the PCC ρ is defined as

$$\rho(X, Y) = \frac{\sum_{i=1}^n (x_i - \bar{x})(y_i - \bar{y})}{\sqrt{\sum_{i=1}^n (x_i - \bar{x})^2 \sum_{i=1}^n (y_i - \bar{y})^2}}, \quad (1)$$

which determines the value between -1 and 1 . For independent two variables, we have $|\rho| = 0$. When $|\rho| > 0.5$, it is typically interpreted as a significant association. $|\rho| = 1$ indicates that two variables have a perfect linear correlation, where positive and negative signs imply increasing and decreasing linear dependence, respectively. Here, we used the absolute value of PCC for convenience.

Kendall's τ correlation coefficient [19] measures the strength of the monotonicity of the relationship between

two variables, which is defined by

$$\tau(X, Y) = \frac{(c - d)}{nC_2}, \quad (2)$$

where c and d are the number of concordant and discordant pairs in (X, Y) , respectively. Given two samples of observations from the combined variable $(X, Y) = \{(x_1, y_1), (x_2, y_2), \dots, (x_n, y_n)\}$, if two sampled pairs are either $x_i > x_j$ and $y_i > y_j$ or $x_i < x_j$ and $y_i < y_j$, it is called a concordant pair. On the other hand, if two samples are either $x_i > x_j$ and $y_i < y_j$ or $x_i < x_j$ and $y_i > y_j$, it is a discordant pair. Hence, Kendall's τ coefficient provides the ordinal association as the proportion of the difference between ordered and disordered pairs to all the possible combinations. As with the PCC, $\tau(X, Y)$ varies from -1 to 1 . If the order of two pairs is randomly distributed, they are monotonically independent, yielding $\tau(X, Y) = 0$. If Y values tend to change with increasing or decreasing X values, the absolute value of Kendall's τ becomes to one.

Meanwhile, mutual information (MI) can estimate and characterize the strength of shared information between data sets. For given two discrete random variables A and B with a joint probability mass function $p(a, b)$ and marginal probability mass functions $p(a)$ and $p(b)$, MI is defined as:

$$I(A; B) = \sum_{a \in A} \sum_{b \in B} p(a, b) \log_2 \frac{p(a, b)}{p(a)p(b)}. \quad (3)$$

Note that MI provides non-negative values, $I(A; B) \geq 0$. If the random variable B is a function of A , $B = f(A)$, $I(A; B)$ diverges. In addition, if A and B have no shared information, $p(a, b) = p(a)p(b)$, then $I(A; B)$ vanishes clearly; they are statistically independent. Refer to more detailed properties in [25].

Suppose that the joint probability distribution $p_{XY}(i, j)$ is approximated by the number of points falling into the i -by- j th bin on the partitioned plane of scattered plots of two time-series data sets X and Y . Then, approximated MI is obtained by the occupied elements in each cell as:

$$I(X; Y)_{k,l} = \sum_{i=1}^k \sum_{j=1}^l \frac{p_{XY}(i, j)}{\log_2 \min \{k, l\}} \log_2 \frac{p_{XY}(i, j)}{p_X(i)p_Y(j)}, \quad (4)$$

where $p_X(i)$ and $p_Y(j)$ are marginal distributions on i -th column and j -th row. In addition, k and l indicate the partition size of X column and Y row, respectively. Because Jensen inequality, $0 \leq I(X; Y)_{k,l} \leq \log_2 \min \{k, l\}$, is satisfied [25], the value in Eq. (4) can be normalized and spans between zero and one.

To overcome a heuristic approach of maximizing MI value for all possible resolution of k -by- l grid [20], three intrinsic properties in Eq. (4) are utilized; they are 1) monotonic convex function, 2) bounded set, and 3) uniformly continuous function, which allows computing Eq. (4) more efficiently and effectively.

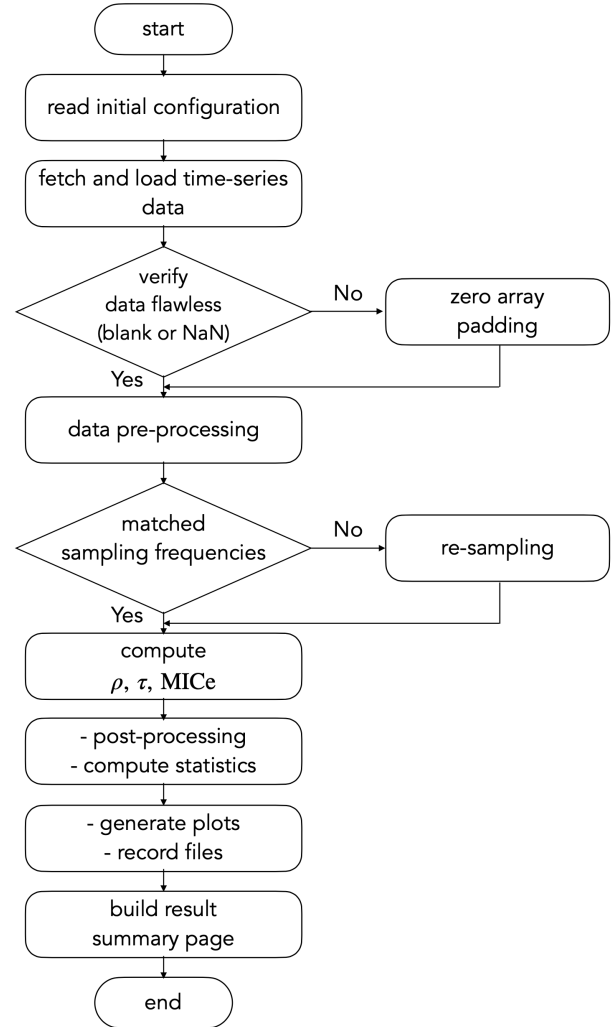


FIG. 1: A flowchart of the CAGMon tool.

B. CAGMon: A Novel Tool for Identifying Correlations

Let S be a n ordered pair-set and $B(n) = n^\alpha$ and the parameter c restricts the total grid size. Here, α is a dimensionless parameter that controls the size of grids and c is a controlling the coarseness of maximizing the discrete grid search. Then, the empirical MIC called MICE is defined as:

$$MICE(X, Y, \alpha, c) = \max_{ab < B(n)} \left\{ \frac{\max I^{[*]}(S, k, l)}{\log_2 \min \{k, l\}} \right\}, \quad (5)$$

where $I^{[*]}(S, k, l)$ denotes the maximized MI in $k \times l$ grids. Note that the coefficient of MICE varies from zero to one. If two time-series data have a clear association, MICE converges to one for sufficiently large data sizes whereas it becomes to zero in the opposite condition. However, even though MICE has a unique performance to extract the complex associations, it was uncertain how

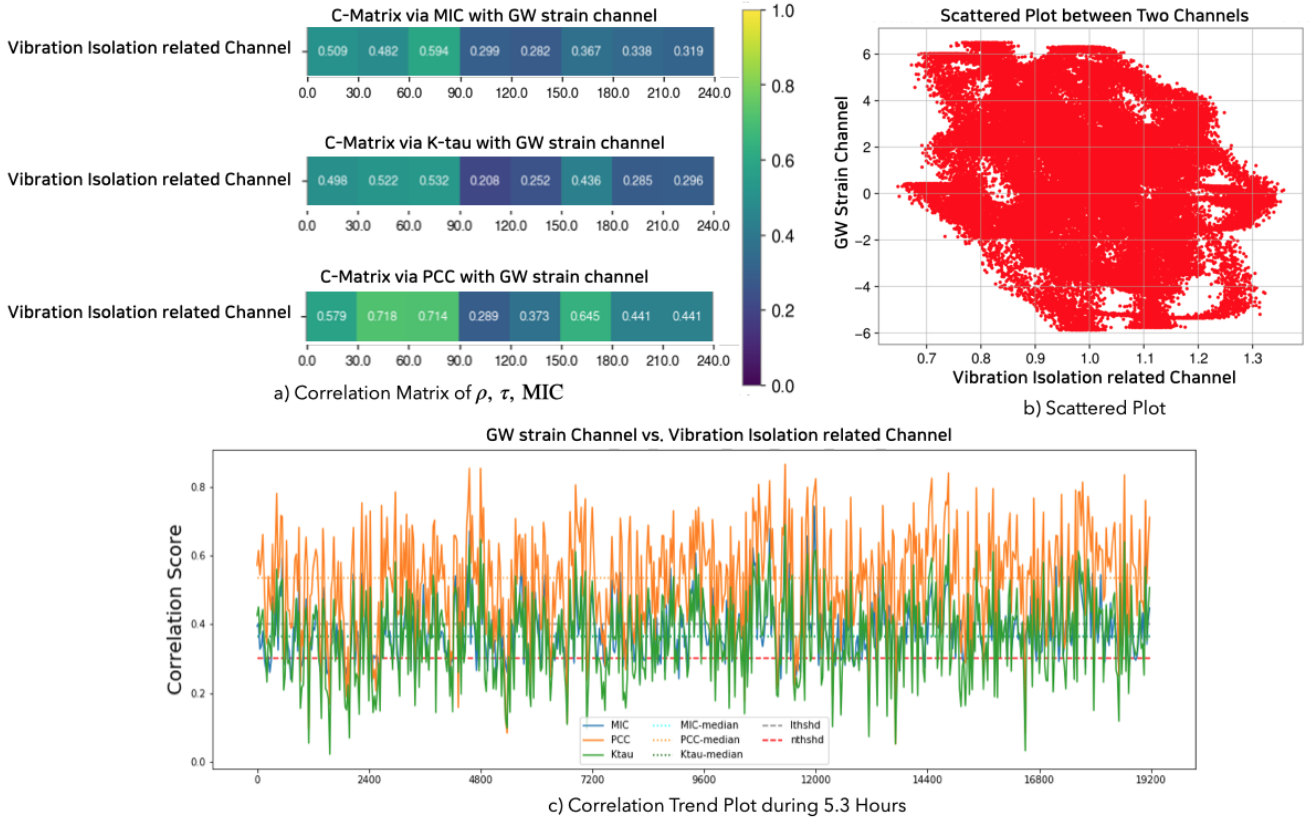


FIG. 2: Exemplary plots provided by the *CAMon* tool: a) correlation matrix plot of ρ , τ , and MIC between primary and auxiliary channels b) scattered plot of both channels (Each relative amplitude is rescaled by its median.) c) correlation trend plot within a certain duration. Here, we demonstrate one of vibration isolation system (VIS) channels among tens of auxiliary channels in the KAGRA GW detector as a simple example.

reliable MICE values can be provided about their correlations in the aspect of the parameter selection. To investigate its reliability, we have determined the relevant parameters of MICE via the statistical power to optimize them. Refer to [26] more details on the optimized parameters of MICE.

We utilize the aforementioned correlation measure indices to identify the data associations between the primary channel and auxiliary channels of GW detectors. Two types of channels are considered as a primary channel to witness of the sensitivity degradation by transient noises: the binary neutron star (BNS) range channel and the strain channel of GW detectors. The BNS range channel is a monitoring channel that represents the volume/orientation-averaged distance based on the GW signals with a matched filtered signal-to-noise ratio (SNR) of 8 from the two $1.4M_{\odot}$ neutron stars in a GW detector [5, 27]. The slowly-moving behavior caused by long-duration noise disturbances in LIGO detector has been investigated via the least absolute shrinkage and selection operator (LASSO) regression, where the BNS range channel was used as a primary channel [14].

To monitor the chronological trend of associa-

tion coefficients between two datasets, we considered a minimal bin of data segment, called *stride*, which represents a piece of an equal interval unit in the whole data segments. For given data sets, aforementioned three correlation coefficients, $\{\rho(X_m, Y_m), \tau(X_m, Y_m), MICE(X_m, Y_m)\}$, are computed for divided subsets of X_m and Y_m by stride. By gathering the sequential coefficients together, we can demonstrate a time-serial trend of the association strength between two channels. In this section, we present a novel tool for identifying and diagnosing the association of two datasets, called *CAGMon*; the workflow and design of the algorithm.

The workflow of *CAGMon* tool is depicted in Fig. 1, which comprises four different stages: i) reading initial configuration, ii) loading time-series data and pre-processing, iii) computing each coefficient and the relevant statistics, and iv) plotting results and building a result summary page. First, the configuration file consists of user-defined parameters, pre-processing options, and general feature of data such as sampling rate, start/end times, and stride. Because each coefficient is computed for each stride of time-series datasets, the

| primary channel | stride(s) | sampling rate(Hz) | data size | α | c |
|-----------------|-----------|-------------------|-----------|----------|-----|
| GW strain | 2 | 4096 | 8192 | 0.5 | 0.7 |
| BNS range | 512 | 16 | 8192 | 0.5 | 7.0 |

TABLE I: The primary channel information and parameters of MICE used in this study: these values are selected by the empirical optimized parameter selection in [26].

tool can only investigate the similar timing coincidence within the same stride bin. Hence, there has a limitation of identifying association for transient noises correlated to noise with a specific frequency. To overcome this limitation, we provide several customized options of data pre-processing, such as high-pass, low-pass, and band-pass filters, for a variety of scalable analyses. In addition, general feature of data comprises a primary channel name, the path of data files, an auxiliary channel list file, segment file, output file type and its save path, and so on. When the time-series data is retrieved from GW frame files, the configuration option refers to the initial configuration file to apply the pre-processing. If time-series data contain either blank or NaN, zero arrays would be padded properly to avoid a computational error. Then, data are re-scaled to have the same data size using the resampling algorithm. The detailed discussion and analyses on the reliability of MICE values, data sample size, and optimal parameters of MICE has been presented in [26]. In this study, we select a set of optimal parameters of MICE presented in Table I.

To monitor the long duration behavior during a few hours or a day, it is reasonable to select the BNS range channel as a primary channel to set up the sampling frequency of 16Hz. Then, it is crucial to perform a pre-processing via high-pass/bandpass filters to focus on targeted frequency band. Whereas if we focus on the short-duration transient noises between GW and auxiliary channels, it is plausible to select two seconds of stride with 4096Hz. Most of all, it is essential to maintain a consistent method for interpreting the result in the whole process of analysis. After computation, a result summary page is built and published automatically, containing the initial configurations, distribution trend plots for each coefficient, ranked summary table, and detailed trend plots for each channel.

III. APPLICATION TO GRAVITATIONAL-WAVE DATA

CAGMon tool was designed to identify and diagnose associated auxiliary channels that influence the primary channel for GW detection, producing a time-sequential correlation trend propagated by instrumental or environmental disturbances. We can estimate a significant association as an excess from the long duration trend of its median value. In this section, we apply *CAGMon* tool to the KAGRA GW data for characterizing and identifying

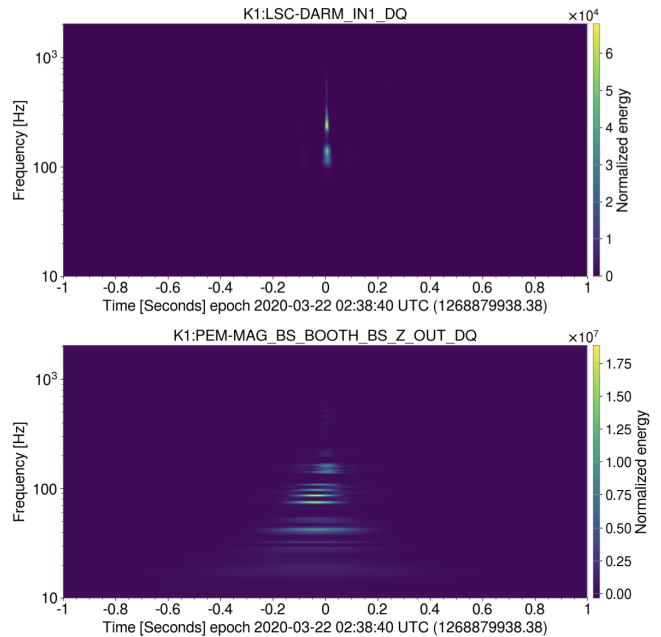


FIG. 3: Omega scan plots of GW interferometer channel (top) and magnetometer at the beam splitter (BS) station (bottom).

associations between channels caused from well-known environmental and instrumental events such as a lightning stroke and an air compressor noises.

A. Magnetic Field Transients from Lightning stroke

First, *CAGMon* tool can be applied to investigate a magnetic field transient noise caused by a lightning stroke event observed by the KAGRA collaboration that was verified by a clear causal relationship between two channels in [28]. A lightning stroke is a locally enormous release of electromagnetic waves, which clearly affects to GW detector by a sudden variance of magnetic fields. KAGRA GW detector was influenced by a lightning stroke at 02:38:40.38 on March 21, 2020 UTC, which was recorded in the GW strain channel and magnetometers. This detection was the first evidence observed by the KAGRA GW detector that the lightning strokes in the atmosphere would be able to affect the underground-based GW detector within the detection range. The data recorded in magnetometer can propagate to the primary channel of the KAGRA GW detector, producing a coincident transient noise in the primary channel with a significant association. Hence, we can infer that there exist a significant causal relationship between the primary channel and the magnetometer-related channels. The omega-scan spectrogram plots based on Q-transform are presented in Fig. 3.

Here, we used the GW interferometer channel as a primary channel and set two seconds of stride with 8192

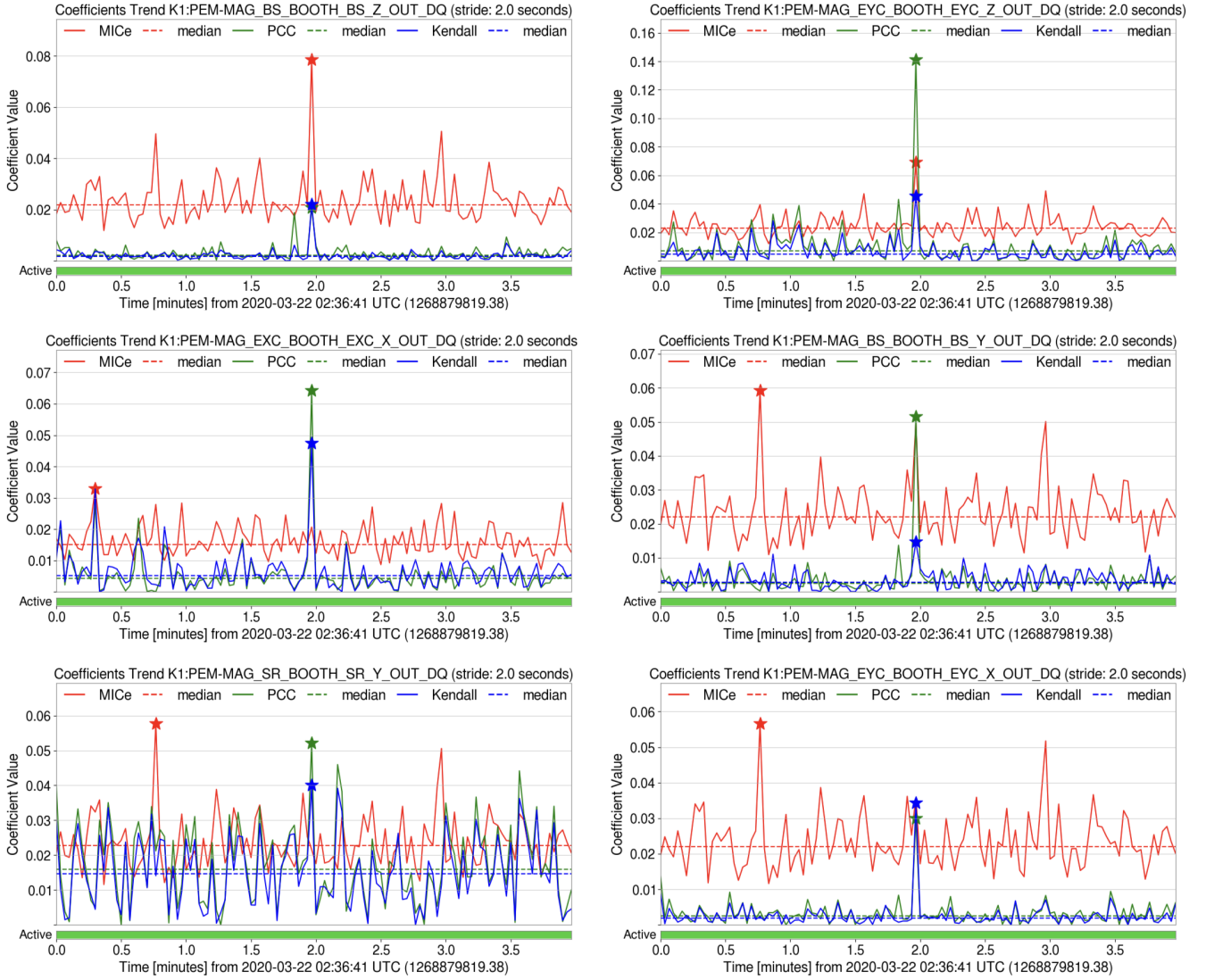


FIG. 4: Correlation trend plot of association between GW interferometer channel and magnetometer associated channels at BS station at the lightning event time. The solid-line and the dashed-line indicate the strength of correlation coefficient and median value, respectively. Here, the star-mark represents the maximum value of (MIC_e, ρ, τ) .

data size to investigate a correlation between short-duration data segments. The mutual correlations between the GW interferometer channel and the magnetometer related channels detects a meaningful signal at the event time of the lightning stroke. Here, correlation trend plots are depicted in Fig. 4, yielding a clear peak signal at the event time of the lightning stroke. It is inferred that the magnetic field noise from the lightning stroke event can propagate and affect the GW interferometer channel. Interestingly, the aspect of each correlation exhibited in Fig. 4 shows that they are linearly or non-linearly correlated with each other for the individual subsystems. The values with significant correlations are much greater than the median values of four minutes duration data segment. In addition, we list the magne-

tometer associated subsystems with a significant correlation of the lightning stroke event in Table II.

B. Periodic Noises from Air compressors

We applied the *CAGMon* tool to the observing run of KAGRA (O3GK run) from April 7, 2020, to April 21, 2020 [30, 31]. Unlike the aforementioned analysis for transient noise, we used the BNS range channel as a primary channel and investigated internal or external influences on the detector's sensitivity during the long period of observational mode. Because data record a minute trend of sensitivity range with around three minutes latency, we set 512 seconds of stride and 8192 of data size. With

| Event time(GPS) | Associated auxiliary channels ^a | MICe | Med(MICe) ^b (10^{-2}) | ρ | Med(ρ)(10^{-2}) | τ | Med(τ)(10^{-2}) |
|---|---|-------|--------------------------------------|--------|----------------------------|--------|----------------------------|
| March 22, 2020 02:38:39-41UTC (1268879937.38 -1268879939.38) | K1:PEM ^c -MAG_BS_BOOTH_BS_Z_OUT_DQ | 0.079 | 2.210 | 0.021 | 0.212 | 0.022 | 0.172 |
| | K1:PEM-MAG_BS_BOOTH_BS_Y_OUT_DQ | 0.050 | 2.210 | 0.052 | 0.250 | 0.015 | 0.275 |
| | K1:PEM-MAG_BS_BOOTH_BS_X_OUT_DQ | 0.026 | 2.188 | 0.040 | 0.266 | 0.001 | 0.197 |
| | K1:PEM-MAG_EXC_BOOTH_EXC_X_OUT_DQ | 0.021 | 1.499 | 0.064 | 0.423 | 0.047 | 0.521 |
| | K1:PEM-MAG_EYC_BOOTH_EYC_Z_OUT_DQ | 0.069 | 2.309 | 0.141 | 0.709 | 0.045 | 0.474 |
| | K1:PEM-MAG_SR_BOOTH_SR_Z_OUT_DQ | 0.022 | 2.271 | 0.052 | 1.595 | 0.040 | 1.458 |

^a All exhibited channels here are related to magnetometers installed in several areas nearby the KAGRA GW detector.

^b The median value was computed for four minutes duration segment.

^c PEM stands for the physical environment monitor that is related to subsystems for sensing environmental changes such as seismometer, magnetometer, accelerometer, and so on [29].

TABLE II: Correlation values of MICe, ρ , and τ at the lightning stroke event time and some associated channels with the magnetometer in the KAGRA GW detector.

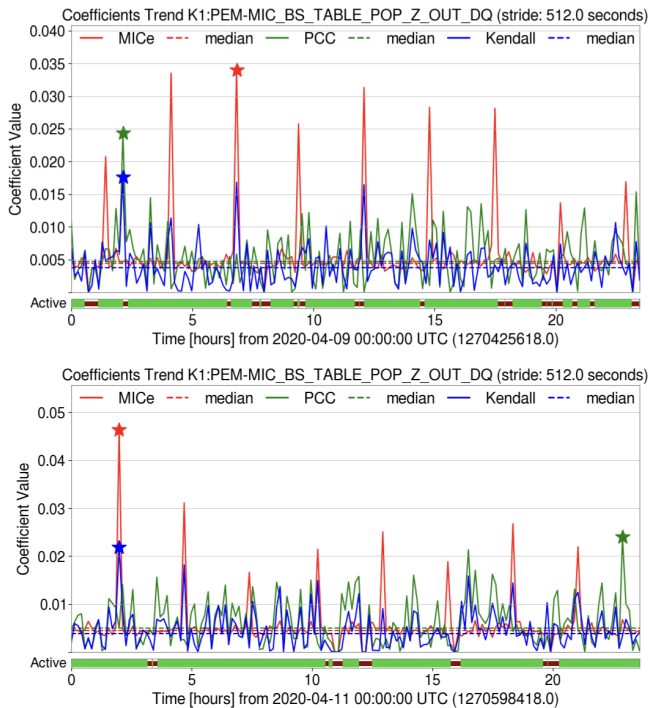


FIG. 5: Correlation trend plots between the BNS range and microphone channels installed in the BS Station POP room on April 9, 2020 (top) and April 11, 2020 (bottom); Relatively strong MICe correlations were repeated for every 2.58 hours.

this configuration, significant correlations were periodically repeated between the BNS range channel and microphone channels at the BS station. These correlated peak signals have a harmonic frequency of 26.5Hz and repeat with a periodicity of 2.58 hours every day. Figure 5 exhibits the correlation trend plots of this periodic behavior using the *CAGMon* tool. In addition, it has been found that the air compressor at the output mode cleaner(OMC) produces periodic vibrations that corre-

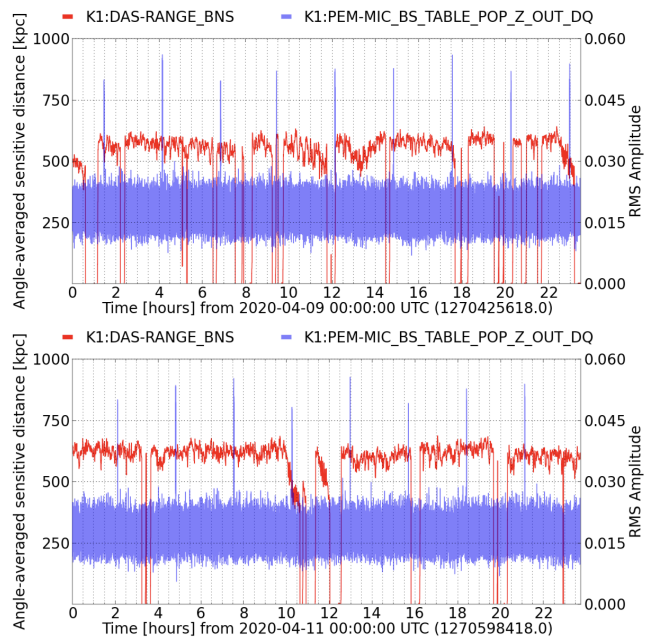


FIG. 6: The BNS range curve experiences a sudden drop as much as about 50kpc owing to the air compressor vibration from OMC station on April 9, 2020 (top) and April 11, 2020 (bottom).

lated through nearby instruments to result in the sudden drop of the BNS range of KAGRA sensitivity curve. The BNS range drop owing to the periodical air compressor noises is demonstrated in Fig. 6. This phenomenon was previously reported during the KAGRA engineering operation and reduced significantly via the installation of the vibration isolation and the soundproof devices in the air compressors. However, the *CAGMon* tool caught this effect clearly even if it had reduced. Consequently, this example indicates that association may exist if the trend of the coefficients is changed regardless of their strength.

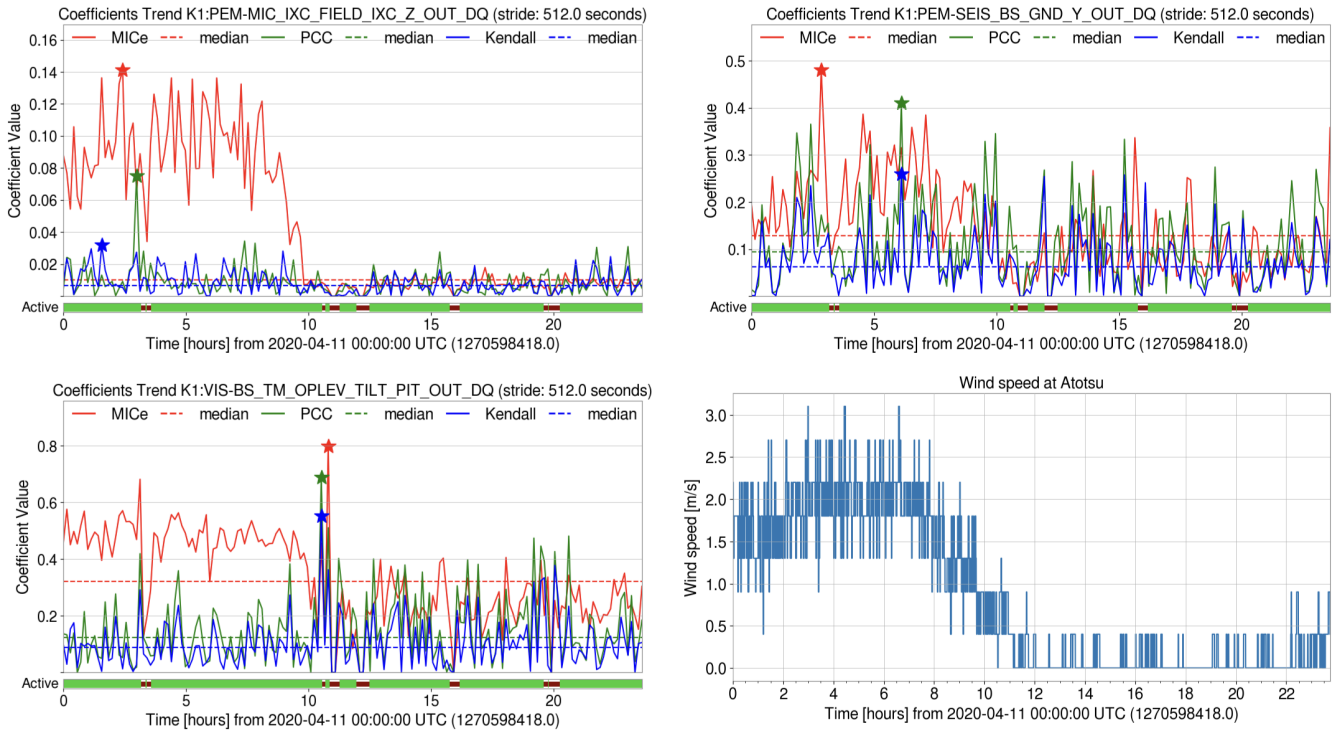


FIG. 7: Correlation trend plots between the BNS range channel and microphone channel installed the initial x-arm tank (top-left), the test mass optical leverage at BS VIS channel (bottom-left), and the y-axis seismometer at BS (top-right). And, the plot of wind speed defined as the average wind speed over two minutes at the entrance of KAGRA (Atotsu) on April 11, 2020 (bottom-right)

C. Glimpse of Acoustic Noise from Winds

Another interesting glimpse via *CAGMon* tool was observed by a clear correlation between the BNS range channel and the microphone/vibration isolation channels. The correlation trend plot exhibits a meaningful association from morning (9 A.M, JST) to evening (7 P.M, JST) everyday in spring season, which is inferred by a relationship with a strong wind power during this time (Fig. 7). Because the KAGRA GW detector is installed in the underground tunnel in the Mt. Ikeno, we infer that this is responsible for the propagation of an acoustic wave noise owing to strong winds between Mt. Ikeno. Fig. 7 exhibits an interesting feature of MICe because this association only was detected by MIC rather than PCC and Ktau; one can infer that the effect of winds can affect non-linearly the KAGRA detector. A possibility of influences by the fluctuating gravity gradient noises in the ground and air around the detector has been reported in [32]. For this reason, it is worth while studying because the seismic coupling and up-conversion effect may affect the GW detection band for the underground detector.

A potential scenario of this effect is considered by a simple simulation of the elastic wave equation in the underground like the KAGRA detector. The wall of the L-shape tunnel in the KAGRA detector consists of the concrete material and air inside the tunnel. The y -arm of

the KAGRA detector is parallel to the slope of the valley in Mt. Ikeno whereas the x -arm is located from the slope to deep inside the mountain. The seismic incident wave generated from the strong winds striking the slope vibrates and propagates then transforms into an acoustic wave inside the tunnel. The acoustic vibration produces sound pressure noise inside the tunnel. Because of the location of both arms in the KAGRA detector, the sound pressure noise level in the y -arm direction is much more severe than that in the x -arm direction due to the attenuation inside the deeper region of the tunnel.

The finite element method (FEM) simulation of the seismic and acoustic waves with a multi-physics configuration and the sound pressure level along x -arm direction in diverse frequencies are shown in Fig. 8.¹ Consequently, the seismic vibration from Mt. slope can propagate to air fluctuation in the tunnel of the KAGRA, which might produce acoustic noises inside the tunnel, which needs to be verified by more accurate simulation and instrumental measurement.

¹ The simulation has been performed by COMSOL-Multiphysics 5.6 with somewhat *ad hoc* parameters and assumptions in order to check the glimpse of the scenario.

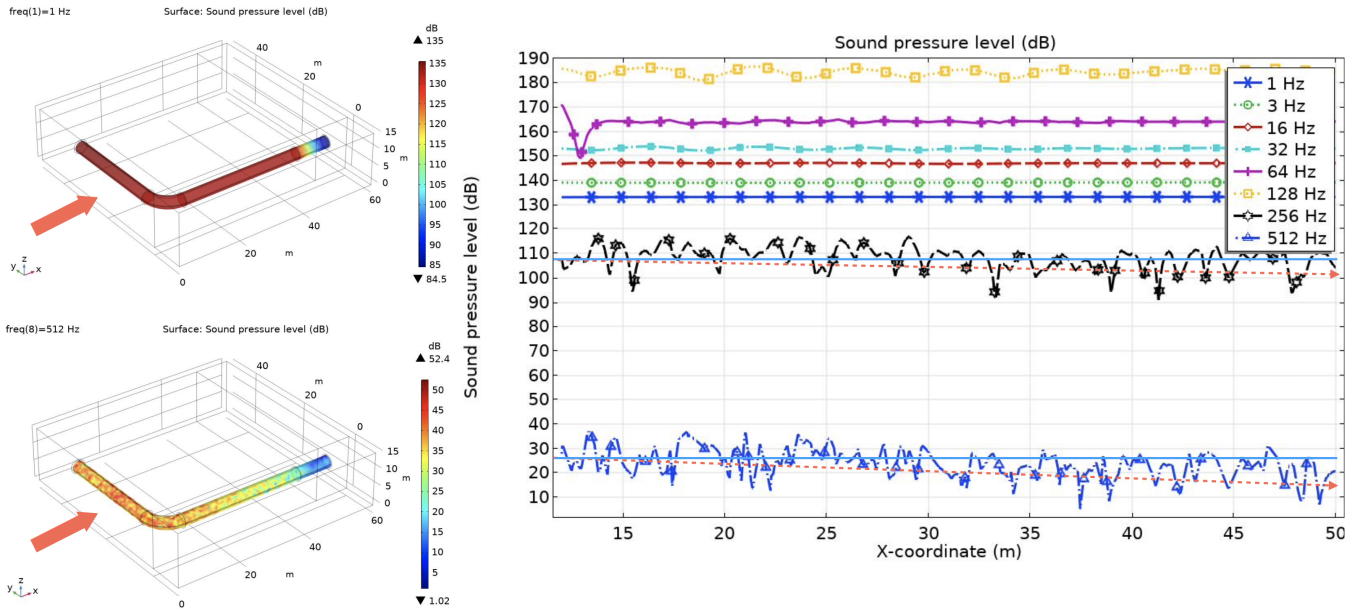


FIG. 8: The simulation of seismic and acoustic wave propagation in the underground tunnel of KAGRA and its x -arm sound pressure level in diverse frequencies. The perfectly matched layer (PML) was applied in the end region of x -arm.

IV. DISCUSSIONS

We developed a novel tool for identifying and diagnosing data association between two variables to investigate presumably correlated events between multi-channels of the GW detectors, called *CAGMon*. In this tool, three linear and non-linear measures, PCC, Ktau, and MIC, were adopted and the optimized parameter selection for MIC was referred in [26].

We applied this tool for the transient and periodic noises caused by a lightning stroke event and an acoustic noise caused by an air compressor in the KAGRA GW detector. Consequently, we verified that several magnetometer associated subsystems influenced by the lightning stroke event have a significant association with the GW strain channel. On the other hand, we found that the sudden detection range reductions in the BNS range curve of the KAGRA detector is associated with the periodic noise in every 2.58 hours appeared in the microphone channels. The noise was identified with a harmonic frequency of 26.5Hz and the evident cause was confirmed by acoustic noises from the air compressor nearby the BS station. Finally, it is observed a glimpse of the wind effect to the underground detector via *CAGMon* tool. In the daytime, air nearby mountains becomes heated and makes relatively strong wind between moun-

tains. This wind hits the ground surface where the detector locates, yielding and propagating microseismic noise and infrasound waves toward the underground detector [33]. Thus, the detector experiences the acoustic and seismic vibrations during the windy time. This scenario seems plausible but needs to verify in various aspects.

Potentially, this study will help to overcome several limitations in the KAGRA detector, and thereby not only improve the noise reduction study but also develop advanced tools and interfaces will contribute to next-generation gravitational-wave telescopes. Furthermore, this tool will help scientists in the GW detection as well as other fields of sciences.

ACKNOWLEDGMENTS

The authors would like to thank Kyujin Kwak, Kyungmin Kim, and Whansun Kim for their helpful discussions and comments. This work was supported by the Basic Science Research Program through a National Research Foundation of Korea (NRF) funded by the Ministry of Education (NRF-2020R111A2054376). Furthermore, this work is partially supported by the NRF grant funded by the Korean government's Ministry of Science and ICT (No. 2019R1A2C2006787, No. 2016R1A5A1013277, No. 2019R1C1C1010571, and No. 2021R1A2C1093059).

[1] B. P. Abbott *et al.* (LIGO Scientific, Virgo), *Phys. Rev. Lett.* **116**, 061102 (2016), arXiv:1602.03837 [gr-qc].

[2] J. Aasi *et al.* (LIGO Scientific), *Class. Quant. Grav.* **32**, 074001 (2015), arXiv:1411.4547 [gr-qc].

- [3] F. Acernese *et al.* (VIRGO), *Class. Quant. Grav.* **32**, 024001 (2015), [arXiv:1408.3978 \[gr-qc\]](#).
- [4] T. Akutsu *et al.* (KAGRA), *Nature Astron.* **3**, 35 (2019), [arXiv:1811.08079 \[gr-qc\]](#).
- [5] B. P. Abbott *et al.* (KAGRA, LIGO Scientific, VIRGO), *Living Rev. Rel.* **21**, 3 (2018), [arXiv:1304.0670 \[gr-qc\]](#).
- [6] M. Punturo *et al.*, *Class. Quant. Grav.* **27**, 194002 (2010).
- [7] B. P. Abbott *et al.* (LIGO Scientific), *Class. Quant. Grav.* **34**, 044001 (2017), [arXiv:1607.08697 \[astro-ph.IM\]](#).
- [8] J. Aasi *et al.* (LIGO Scientific, VIRGO), *Class. Quant. Grav.* **32**, 115012 (2015), [arXiv:1410.7764 \[gr-qc\]](#).
- [9] B. P. Abbott *et al.* (LIGO Scientific, Virgo), *Class. Quant. Grav.* **33**, 134001 (2016), [arXiv:1602.03844 \[gr-qc\]](#).
- [10] P.-J. Jung, K.-Y. Kim, J. J. Oh, S. H. Oh, E. J. Son, and Y.-M. Kim, *J. Korean Phys. Soc.* **73**, 1197 (2018), [arXiv:1806.08912 \[gr-qc\]](#).
- [11] L. Nuttall *et al.*, *Class. Quant. Grav.* **32**, 245005 (2015), [arXiv:1508.07316 \[gr-qc\]](#).
- [12] F. Robinet, N. Arnaud, N. Leroy, A. Lundgren, D. Macleod, and J. McIver, (2020), [arXiv:2007.11374 \[astro-ph.IM\]](#).
- [13] E. J. Son, W. Kim, Y.-M. Kim, J. McIver, J. J. Oh, and S. H. Oh, *J. Korean Phys. Soc.* **78**, 878–885 (2021).
- [14] M. Walker, A. F. Agnew, J. Bidler, A. Lundgren, A. Macedo, D. Macleod, T. J. Massinger, O. Patane, and J. R. Smith, *Class. Quant. Grav.* **35**, 225002 (2018), [arXiv:1807.02592 \[astro-ph.IM\]](#).
- [15] E. Cuoco, J. Powell, M. Cavaglià, K. Ackley, M. Bejger, C. Chatterjee, M. Coughlin, S. Coughlin, P. Easter, R. Essick, H. Gabbard, T. Gebhard, S. Ghosh, L. Haegel, A. Iess, D. Keitel, Z. Márka, S. Márka, F. Morawski, T. Nguyen, R. Ormiston, M. Pürrer, M. Razzano, K. Staats, G. Vajente, and D. Williams, *Machine Learning: Science and Technology* **2**, 011002 (2020).
- [16] S. Bose, B. Hall, N. Mazumder, S. Dhurandhar, A. Gupta, and A. Lundgren, *J. Phys. Conf. Ser.* **716**, 012007 (2016), [arXiv:1602.02621 \[astro-ph.IM\]](#).
- [17] P. Ajith, T. Isogai, N. Christensen, R. X. Adhikari, A. B. Pearlman, A. Wein, A. J. Weinstein, and B. Yuan, *Phys. Rev. D* **89**, 122001 (2014), [arXiv:1403.1431 \[gr-qc\]](#).
- [18] K. Pearson, *Biometrika* **13**, 25 (1920).
- [19] M. G. Kendall, *Biometrika* **30**, 81 (1938).
- [20] D. N. Reshef, Y. A. Reshef, H. K. Finucane, S. R. Grossman, G. McVean, P. J. Turnbaugh, E. S. Lander, M. Mitzenmacher, and P. C. Sabeti, *Science* **334**, 1518 (2011).
- [21] Y. A. Reshef, D. N. Reshef, H. K. Finucane, P. C. Sabeti, and M. Mitzenmacher, *Journal of Machine Learning Research* **17**, 1 (2016).
- [22] D. N. Reshef, Y. A. Reshef, P. C. Sabeti, and M. Mitzenmacher, *The Annals of Applied Statistics* **12**, 123 (2018).
- [23] T. Akutsu *et al.*, *Progress of Theoretical and Experimental Physics* **2021**, 05A101 (2020).
- [24] K. Kokeyama (KAGRA), in *3rd World Summit on Exploring the Dark Side of the Universe* (2020).
- [25] T. M. Cover and J. A. Thomas, *Elements of information theory*, 2nd ed. (A Wiley-Interscience publication, 2006).
- [26] P. Jung, S. H. Oh, Y.-M. Kim, E. J. Son, and J. J. Oh, (2021), [arXiv:2107.03516 \[astro-ph.IM\]](#).
- [27] L. S. Finn and D. F. Chernoff, *Phys. Rev. D* **47**, 2198 (1993).
- [28] T. Washimi, T. Yokozawa, M. Nakano, T. Tanaka, K. Kaihotsu, Y. Mori, and T. Narita, *Journal of Instrumentation* **16**, P07033 (2021).
- [29] T. Akutsu *et al.*, *Progress of Theoretical and Experimental Physics* **2021**, 05A102 (2021).
- [30] R. Abbott *et al.* (LIGO Scientific, VIRGO, KAGRA), (2022), [arXiv:2203.01270 \[gr-qc\]](#).
- [31] H. Abe *et al.* (KAGRA), (2022), [arXiv:2203.07011 \[astro-ph.IM\]](#).
- [32] T. Creighton, *Class. Quant. Grav.* **25**, 125011 (2008), [arXiv:gr-qc/0007050](#).
- [33] G. Chimonas, *Journal of Atmospheric Sciences* **34**, 806 (1977).